# Rapid and efficient ultrasonic assisted adsorption of diethyl phthalate onto $Fe^{II}Fe_2^{III}O_4$@GO: ANN-GA and RSM-DF modeling, isotherm, kinetic and mechanism study

Ali Azari[a,b,c], Mohammad Hassan Mahmoudian[d], Maryam Hazrati Niari[e], Ismail Eş[f], Emad Dehganifard[g,h], Amin Kiani[i], Allahbakhsh Javid[j,*], Hossein Azari[k], Yadolah Fakhri[l], Amin Mousavi Khaneghah[m,**]

[a] Department of Environmental Health Engineering, School of Public Health, Kashan University of Medical Sciences, Kashan, Iran
[b] Students' Scientific Research Center (SSRC), Tehran University of Medical Sciences, Tehran, Iran
[c] Department of Environmental Health Engineering, School of Public Health, Tehran University of Medical Sciences, Tehran, Iran
[d] Department of Environmental Health Engineering, School of Public Health, Qom University of Medical Sciences, Qom, Iran
[e] Department of Environmental Health Engineering, School of Public Health, Jundishapur University of Medical Sciences, Ahvaz, Iran
[f] Department of Material and Bioprocess Engineering, School of Chemical Engineering, University of Campinas, Campinas, SP, Brazil
[g] Department of Environmental Health Engineering, School of Public Health, Alborz University of Medical Sciences, Karaj, Iran
[h] Research Center for Health, Safety and Environment (RCHSE), Alborz University of Medical Sciences, Karaj, Iran
[i] Department of Public Health, School of Public Health, Fasa University of Medical Sciences, Fasa, Iran
[j] Environmental and Occupational Health Research Center, Shahroud University of Medical Sciences, Shahroud, Iran
[k] Qom University of Medical Sciences, Qom, Iran
[l] Student Research Committee, Department of Environmental Health Engineering, School of Public Health and safety, Shahid Beheshti University of Medical Sciences, Tehran, Iran
[m] Department of Food Science, Faculty of Food Engineering, State University of Campinas (UNICAMP), Monteiro Lobato, 80, Caixa Postal: 6121, CEP: 13083-862 Campinas, São Paulo, Brazil

ARTICLE INFO

ABSTRACT

Herein, an ultrasonic assisted dispersive magnetic solid-phase adsorption method along with a high-performance liquid chromatography system for the diethyl phthalate (DEP) removal was developed. In this regard, magnetic iron oxide/graphene oxide (MGO) nanocomposites were prepared by a simple and effective chemical co-precipitation method, followed by nucleation and growth of nanoparticles. The structure and morphology of MGO was identified by Transmission electron microscopy (TEM), Scanning electron microscopy (SEM), Energy dispersive X-ray (EDX) spectroscopy X-ray diffraction (XRD), Vibrating sample magnetometer (VSM), Fourier transform infrared spectroscopy (FT-IR), X-ray photoelectron spectroscopy (XPS) and N2 adsorption-desorption techniques. The interactive and main effect of parameters such as pH, adsorbent dosage, sonication time and concentration of DEP involved in the adsorption process were set within the ranges 3.0–11.0, 0.10–0.50 g L$^{-1}$, 1–5 min, 5–10 mg/L, respectively. Root means square error (RMSE), mean absolute error (MAE), absolute average deviation (AAD), and coefficient of determination ($R^2$) was employed to examine the applicability of the response surface methodology (RSM) and artificial neural network (ANN) models for the description of experimental data. Compared to RSM, the ANN showed a more accurate performance for modeling the process of DEP adsorption. Using genetic algorithm-ANN, optimum conditions were set to 5.38, 334.7 mg/L, 3.723 min and 4.21 mg/L for pH, adsorbent dose, sonication time and concentration of DEP, respectively. Under the optimized conditions, the maximum adsorption capacity and adsorption factors were 116.933 mg/g and 100%, respectively, while the relative standard deviations (RSDs) was < 1.6% ($N = 5$). The isotherm models display that the Langmuir has the best fit with the equilibrium data, and adsorption kinetics followed the pseudo-second-order model. The thermodynamic results confirmed that the sorption was endothermic and occurred spontaneously. The results exhibited that MGO has excellent potential as an adsorbent for the removal of phthalates from the contaminated water.

* Correspondence to: A. Javid, Department of Environmental Health Engineering, School of Public Health, Shahroud University of Medical Sciences, Shahroud, Iran.
** Correspondence to: A.M. Khaneghah, Department of Food Science, Faculty of Food Engineering, University of Campinas, Campinas, SP, Brazil.
E-mail addresses: cavid_a@outlook.com (A. Javid), mousavi@unicamp.br (A. Mousavi Khaneghah).

## 1. Introduction

Recently, the emission of next-generation contaminants so-called emerging contaminants (ECs) such as endocrine disrupting chemicals (EDCs), which require more legislative actions, has gained attention of both scientific communities as well as general public [1]. Among the ECs, phthalate acid esters (PAEs or phthalates) have a broad range of industrial use such as industrial plastics, cosmetics, pharmaceutics, and food packaging [2–4].

Diethyl phthalate (DEP) as the representative of the PAEs family widely used as a solvent to maintain color, improved flexibility, durability, and workability in plastic as well as in several cosmetic and consumable products [5]. Due to possible migration, DEPs can be released from the product and cause some adverse effects since they present endocrine disrupting and carcinogenic properties; therefore, many countries have either decreased the upper concentration limit or completely restricted the use of PAEs in specific products with regulation and legislation. Besides, the United States Environmental Protection Agency (EPA) established that DEP is considered priority toxic contaminants [6,7]. Although the global and regional regulations have become stricter, recent investigations showed that these compounds are still found at dangerous concentrations in water and soil. In this regard, monitoring and removal of these contaminants present at trace levels from different environmental matrices are crucial for human health protection and environmental control [8]. In the past decades, different physicochemical treatment methods, including biological treatment [9], photocatalysis [10], and coagulation-flocculation [11] have been employed to remove DEPs from industrial effluents. Nevertheless, these methods present disadvantages, such as high operating costs and generation of toxic secondary effluent and by-products [12].

Review of past reports on remediation of DEP polluted water has shown that adsorption technology has proved to be the most effective option due to high-performance and easy operation for eliminating waste from soils and waters [13]. Khan et al. [14] have investigated the adsorption of phthalic acid and diethyl phthalate using ZIF-8 and reported ZIF-8 was effective in adsorbing DEP from water solution at pH = 3.5. In another study, Wu et al. [15] have investigated the adsorption of diethyl phthalate to clay minerals and obtained > 70% removal at an operating pH of 8.8 within 1 h of time. Furthermore, recent studies also confirmed that the adsorption process is a suitable technique for DEP removing from the aquatic environment [16–18].

Despite the development of various adsorbents for DEP uptake, the carbon-based adsorbents such as graphene oxide (GO) has had more promising results. Nontoxicity, excellent physicochemical and mechanical properties, stability, uniform shape with unique two-dimensional structure (as the single layer form of graphite) and high surface area are only part of the GO features as adsorbent [19–21]. The results of Lu's study on phthalic acid esters (PAEs) adsorption by GO and RGO can confirm the high efficiency of carbonaceous nanomaterials in the removal of DEP [22]. They reported that > 90% of the DEP could be removed by the GO-adsorption process, which is a promising and significant amount. Notwithstanding the mentioned advantages of GO, its laborious separation, and recovery from solution, which might result in secondary pollution, led the researchers to encourage to modify GOs with magnetic composites [23,24]. Therefore, magnetic composites such as $Fe_3O_4$ are utilized as a source of iron graft on GO to facilitate phase separation of magnetic graphene oxide (MGO) by an external magnetic field [25].

In another side, ultrasound irradiation is considered to be a popular technique to accelerate any chemical process owing to the occurrence of acoustic cavitations. When pressure waves propagate through the liquid, it yields to formation, growth, and collapse of micro size bubbles which enhance the mass transfer of adsorbate onto the solid adsorbent surface in an adsorption system. Moreover, in the adsorption process ultrasound irradiation can enhance the mass transfer by breaching the affinity between adsorbate and adsorbent through convection pathway

[26,27]. As a result, ultrasound assisted adsorption process can lead to the occurrence of faster equilibrium of adsorption process reducing the contact time effectively as compared to other conventional adsorption processes [28]. Wang et al. [29] reported that ultrasound improved the adsorption rate in the adsorption of polyphenols with XAD-16. Dorabei et al. [30] found that ultrasound could both raise adsorption rate and shorten equilibrium time of Pb(II), Cd(II), Ni(II) and Cu (II) ions using GO. Zhang et al. [31] demonstrated that the impact of ultrasound on Congo red desorption was positive at low temperature.

Another critical point in the design of novel purification systems is the optimization of variables (principally interaction and residual) and low reagent use that permits the efficient simulation of industrial-scale treatments in laboratory conditions. The traditional optimization techniques are time-consuming and laborious since they allow the investigation of one parameter each time while requiring a high content of reagent use [32]. Therefore, it becomes impossible to understand the whole process without conducting a high number of experiments. However, these limitations can be easily overcome using response surface methodology [33].

According to the fact that no study has been conducted on the performance of MGO-US system in the adsorption of DEP compound, and considering that the modeling and optimization of DEP adsorption by ANN-GA and RSM-DF approaches has not been investigated, in the present study for the first time, MGO assisted with ultrasound waves (MGO-US) as a hybrid system in the removal of DEPs has been studied and effective factors in the process are optimized. In fact, the objectives of this study are summarized as follows: Synthesis of MGO nanoparticles (MGO-NPs) and characterization of its properties via SEM, EDX mapping, XRD, TEM, VSM, FTIR, SEM, and $N_2$ adsorption-desorption techniques, Determination the mutual and individual effects of important variables i.e. sonication time, pH, initial DEP concentration and adsorbent dosage on removal process, Optimization the removal efficiency of DEP by central composite design (CCD) using the desirability function (DF) and artificial neural network (ANN) combined by genetic algorithm (GA) as maximize criterion of the response, Compare the results obtained from DF and GA methods optimization with actual condition and, Study adsorption isotherms, kinetics and thermodynamic of DEP removal under optimized conditions.

## 2. Material and methods

### 2.1. Reagents and instrumental

Reagents and instruments used in this study were given in Supplementary Material Text 1.

### 2.2. Synthesis of MGO adsorbent

The Graphene Oxide (GO) and Magnetic $Fe_3O_4@GO$ (MGO) synthesis procedure in detail is provided on Supplementary Material Text 2.

### 2.3. Ultrasound-assisted adsorption procedure

100 mL of Erlenmeyer flasks containing 25 mL of DEP solution at varying concentrations were used for adsorption experiments. The optimization process was conducted by varying parameters in the range of pH 3.0–11.0, initial DEP concentration 2.0–10.0 mg/L, MGO dose 0.1–0.5 g L$^{-1}$ and sonication time 1.0–5.0 min. All the parameters were tested at temperature 25 ± 5 °C. Residual DEP concentration in each solution was analyzed at the regular time interval. All the experiments were performed in duplicate, and the data analysis was employed using average values. The amount of DEP adsorbed onto the MGO, and the adsorption efficiency (%) was calculated by the following equations:

$$q = \frac{(c_0 - c_e) \times V}{m} \tag{1}$$

$$\text{DEP adsorption (\%)} = \frac{(c_0 - c_e)}{c_0} \qquad (2)$$

where q (mg/ g): adsorbed DEP concentration; $C_o$ and $C_e$ (mg/ L): initial concentration of DEP and concentration of DEP in solution at equilibrium, respectively; V (L) is total solution volume; m (g) is the amount of MGO. The adsorption isotherms were analyzed using different initial DEP concentration between 2 and 10 mg/ L at the optimum specified condition. The kinetics was studied over pre-determined sonication time intervals with a total analysis time of 5 min at optimum conditions. The coefficient of determination ($R^2$) and the chi-square ($\chi^2$) test was employed to determine the model that fits best with the experimental data (Eq. (3)).

$$X^2 = \sum \frac{(q_{e.\,exp} - q_{e.cal})^2}{q_{e.cal}} \qquad (3)$$

where $q_{e,exp}$, and $q_{e,cal}$ are experimental and calculated adsorption capacities, respectively. The smaller $X^2$ value indicates that data acquired from the model are closer to the experimental data. Thermodynamic studies were conducted in optimized conditions at a temperature varying from 293 to 323 K as well.

### 2.4. Experimental design

#### 2.4.1. Principle of central composite design

In this work, DEP adsorption efficiency (%) was performed by CCD with four factors, i.e., initial pH ($X_1$), DEP concentration ($X_2$, mg $L^{-1}$), adsorbent dose ($X_3$, mg) and sonication time ($X_4$, min) at five levels using the Design-Expert® software V.10 according to 21 experimental runs. Table S1 shows the experimental design points in matrix form for the CCD [22]. The correlation between the coded and actual values was described based on the equation (Eq. (4)) used in the previous study [26].

$$Z_i = \frac{X_i - X_0}{\Delta X_i} \qquad (4)$$

where $Z_i$ is the dimensionless independent variable, $X_i$ and $X_0$ are the real values of the independent variable at the current and central points, with the step change of $\Delta X_i$. Following the second-order polynomial model (Eq. (5)) was used to define the mathematical relationship between the independent parameters:

$$Y = b_0 + \sum_{i=1}^{n} b_i x_i + \sum_{i=1}^{n} b_{ii} x_i^2 + \sum_{i=1}^{n-1} \sum_{j=i+1}^{n} b_{ij} x_i x_j \qquad (5)$$

where $Y$ is the DEP adsorption efficiency; $x_i$ and $x_j$ are coded values of the factors (i and j range from 1 to $k$); $b_0$ is the intercept coefficient of model; $b_j$, $b_{jj}$, and $b_{ij}$ are interaction coefficients of linear, quadratic, and the second-order terms, respectively; $n$ is the number of independent parameters ($n = 4$ in this study). The multiple regressions and the significance of regression coefficients were used to analyze experimental records. Modeling was started with a quadratic model involving linear, squared, and interaction terms and the model adequacies were investigated concerning the values of $R^2$, adjusted $R^2$, and prediction error sum of squares (PRESS). The significant terms in the model have been discovered through analysis of variance (ANOVA) for each response, and ANOVA table was made. Statistical calculations were created by using regression coefficients to generate contour plots from the regression models.

#### 2.4.1.1. Optimization of CCD by desirability function approach (CCD-DF). Optimization of the CCD method by DF approach is presented in Supplementary Material Text 3.

#### 2.4.2. Artificial neural network model (ANN)

A three-layer feed-forward neural network model with back propagation learning was constructed for DEP adsorption modeling with Matlab v. 2015a mathematical software. A tangent sigmoid transfer function (tansig) and linear transfer function (purelin) respectively at the hidden layer and output layer built up to forecast and simulate DEP adsorption using MGO. For this purpose, all experimental data were allocated randomly into three groups (70%, for the training set, 15% for the validation set and 15% of the data for the test set). The strong connections between inputs, hidden, and output layers were correlated by using parameters of ANNs (weights (w) and biases (b)). Same as Table S1, four parameters, including initial pH, DEP concentration, adsorbent dose, and sonication time, were chosen as input layers. The results were expressed in one neuron as DEP adsorption in the output layer (target). The complete data were normalized between 0 and 1 due to increasing the numerical stability (accuracy index) of the model construction and produce data with unity standard deviation. Data (indexed by xi) are adapted to normalized value (x normal) as follows:

$$X_{normal} = \frac{0 \cdot 8 (X_i - X_{min})}{X_{max} - X_{min}} + 0 \cdot 1 \qquad (7)$$

where $X_{max}$ and $X_{min}$ are the maximum and minimum actual experimental data, respectively.

Various training algorithms (Levenberg-Marquardt, Fletcher-Reeves conjugate gradient backpropagation, scaled conjugate gradient) were tested by varying the number of neurons as well as training the network to select the optimal architecture based on the minimization of the performance MSE function. The importance of input parameters in the ANN model was calculated according to the Garson equation [27].

#### 2.4.2.1. Optimization of ANN by genetic algorithm approach (ANN-GA). The optimization of ANN by genetic algorithm approach details are given in Supplementary Material Text 4.

#### 2.4.3. Comparison of RSM and ANN model

The comparison of the goodness of fitting (accuracy), estimation capabilities and optimization abilities of the proposed ANN and RSM models evaluated by the descriptive analysis, coefficient of determination ($R^2$), root mean square error (RMSE), mean absolute error (MAE) and absolute average deviation (AAD). Details of mentioned analyses calculation have been fully reported in the previous literature.

## 3. Results and discussions

### 3.1. Characterization of MGO

#### 3.1.1. Scanning and transmission electron microscope (SEM and TEM)

The morphological and structural analyses of $Fe_3O_4$ NPs, GO, and MGO was investigated by SEM and TEM. Fig. S2a showed the SEM image of $Fe_3O_4$ NPs, which suggested that the formation of nanoparticles is nearly uniform and spherical. The more detailed structure on the $Fe_3O_4$ NPs was given in TEM image. The transparent sheets which were plenty of wrinkles with the smooth surfaces were GO (Fig. S2b). In contrast, The MGOs presented a sheet-like structure with reduced wrinkles compared to GOs. This situation could be attributed to the possible exfoliation process during the production of MGOs. It can be observed that the $Fe_3O_4$ NPs are mostly monodisperse with a size ranging from 25 to 40 nm as estimated from the TEM image in Fig. S2c. NPs are distributed on these flake-like GO sheets containing a considerable amount of void spaces. In fact, the GO can reduce or eliminate the aggregation of $Fe_3O_4$ NPs, which can be advantageous for the adsorption process. The images of MGO obtained from TEM agreed with the SEM result, revealing that the aggregation of $Fe_3O_4$ NPs was prevented by iron oxide dispersion on GO. The average particle size of the MGO was determined to be close to 30 nm, which was also in accordance with the value obtained from the Scherrer equation in the X-ray diffraction pattern (32 nm). Fig. S2e–h shows the micrographs of

the 5, 10, 15 and 20 wt% $Fe_3O_4$ in the texture of MGO, respectively. Compared to the GO alone (Fig. S2a), $Fe_3O_4$ NPs were deposited onto GO surfaces of the MGO nanocomposites. A significant reduction in the size of MGO was also observed for the 10 wt% $Fe_3O_4$ NPs loading, calculated from 1 to 1.9 nm. In contrary, for the > 10 wt% $Fe_3O_4$ NPs loading, the magnetic NPs agglomerated on the GO surface, resulting MGO size is thicker than the GO alone. This observation suggests that the low loading of $Fe_3O_4$ NPs prevented severe aggregation, which also led to a more uniform distribution of NPs over the GO planes. Morphological structure of MGOs may vary depending on the functionalization material to give magnetic characteristics. Our findings were in accordance with the morphological characteristics of the magnetic GO using $Fe_3O_4$ NPs produced in previous studies [34]. However, when GO surface was functionalized with $NH_2$ magnetic nanoparticles, the mean diameter of the particles was found to be 50 nm, which is slightly bigger than GO functionalized with $Fe_3O_4$ NPs, and presented a good spherical shape [35,36].

### 3.1.2. Fourier transform infrared spectrometer (FTIR)

The FTIR spectra of GO and MGO are shown in Fig. S3. Several characteristic peaks of GO, i.e., C=O stretching (from carbonyl and carboxyl groups) at 1672 cm$^{-1}$, aromatic C=C resulted from skeletal vibration from unoxidized graphitic domains at 1618 cm$^{-1}$, and alkoxy C–O (1102 cm$^{-1}$) indicate successful oxidation of graphite. Furthermore, the broad absorption band from 3372 to 3604 cm$^{-1}$ is attributed to the O–H stretching vibrations in GO texture and the peak observed at 1386.1 cm$^{-1}$ be allotted to the combination of C–O (carboxy) stretching vibration and deformation vibration of hydroxyl groups [28]. The strong band appearance at 500–600 cm$^{-1}$ differs GO from the MGO in which it denoted the presence of Fe–O indicating that iron has been oxidized into $Fe_3O_4$. As can be seen the corresponding peak to υ(C=O) of –COOH at 1672 cm$^{-1}$ on GO structure shifts to 1594 cm$^{-1}$ because of –COO formation after $Fe_3O_4$ NPs loading process. The stretching vibration of Fe–O bond appears at 500–650 cm$^{-1}$ in $Fe_3O_4$ NPs ref. (bulk $Fe_3O_4$) Shifted to higher wavenumbers of 701 cm$^{-1}$ in MGO. It may be due to that magnetite NPs is bound to the –COO on the GO structure [37].

### 3.1.3. Vibrating sample magnetometer (VSM)

The magnetization curve of MGO is S-like curves (Fig. S4). The magnetic remanence of the MGO was close to zero (0.144 emu g$^{-1}$), indicating that the sample exhibit superparamagnetic characteristics. The specific saturation magnetization (Ms) of the MGO is 76.2 emu g$^{-1}$ was found to be smaller than the previously reported value of $Fe_3O_4$ NPs ref. (bulk $Fe_3O_4$) of 87 emu g$^{-1}$ [38]. The decrease in Ms value could be associated with the smaller size of the $Fe_3O_4$ NPs than MGO and low amount of magnetite loaded on GO, which is estimated at 10 wt%. However, it was shown that the specific Ms value of 16.3 emu$^{-1}$ was sufficient to separate the solution with a magnet and employ this magnetic adsorbent used in wastewater treatment [39,40]. Meanwhile, GO also has very negligible magnetic property, which reduces the Ms value of MGO. Dispersion and magnetically separable of MGO under external magnetic field reveal MGO was dispersed in deionized water and a stable black suspension was given followed by 2 min sonication (Fig. S4d). Nevertheless, after approximating a magnet to the glass vial, MGO was attracted toward the magnet rapidly (< 10 s), and the solution became clearly transparent. In the next step, attraction and re-dispersion ability of MGO investigated. After the removal of the external magnetic field and sonication process, MGO can be rapidly dispersed again. The results show efficient water dispersion and magnetic separation properties for effective separation. It was previously reported that the saturation magnetization of the magnetic GOs depends on the size of the particles. The magnetic GOs with the size of 6 nm had a smaller saturation magnetization comparing to the ones with a diameter of 18 nm [41]. This situation could also be attributed to the presence of organic ligands on the surface of the nanoparticles used to functionalize GOs [42].

### 3.1.4. X-ray diffraction (XRD)

XRD was employed to analyze the crystal structure of both GO and MGO. Fig. S5 shows the XRD diffractogram of GO and MGO. A typical diffraction peak appeared at 2θ = 11.5° with an index (001) corresponding to the GO [43]. The particle size was found to be ~28.5 nm according to the calculation done using Scherrer equation. The peaks at 2θ of 27.45°, 35.4°, 52.3°, 63.51°, and 66.35°, which were corresponding to the (2 2 0), (3 1 1), (4 0 0), (4 2 2), and (5 1 1), are consistent with the standard XRD data for the inverse spinel structure $Fe_3O_4$ with lattice constants of a = 8.397 A° (JCPDS file no. 19-0629). The spectrum of MGO showed the characteristic peak of Fe at 2θ ≈ 27.3° (111), 35.4° (311), 53.1° (400), 63.7° (422) and 66.5° (440). The data confirmed the presence of the $Fe_3O_4$ NPs in MGO. More specifically, we expect that $Fe_3O_4$ NPs were chemically bound to the free COO- groups present on GO surface. From Scherer formula, the average particle size of MGO is estimated as ~31.8 nm. Meanwhile can be seen from Fig. S5a (MGO) diffractive peaks of $Fe_3O_4$ are broadened, implying that the crystallite sizes of magnetic particles are quite small. Moreover, no alteration in the crystal structure of $Fe_3O_4$ NPs was observed after their assembly on GO. These findings are also consistent with the TEM analysis.

### 3.1.5. $N_2$ sorption-desorption

To determine the pore size distribution, the porous capacity of MGO (to the uptake of Nitrogen gas) and to investigate the effect of $Fe_3O_4$ (10 wt%) loading in textural of GO, $N_2$ adsorption-desorption isotherm was calculated and results are shown in Fig. S5b. According to the IUPAC (International Union of Pure and Applied Chemistry) guidelines, the hysteresis loop of MGO is fitted to the H3 type and IV characteristic curves. These results reveal that the MGO nanocomposites are characterized by mesoporous structures. Type H3 hysteresis loop presented the random distribution of pores and interconnection of pores systems. BET surface area was measured using the specific surface area of the as-prepared material according to Brunauer–Emmett–Teller (BET) theory. The BET surface area (corresponds to the BET equation) of the MGO composite is shown in Fig. S5c. The specific surface area of GO and MGO was found to be 421 and 409 m$^2$ g$^{-1}$. DFT model applied to calculate the pore size distribution curves of GO and MGO. The Barrett-Joyner-Halenda (BJH) desorption average pore diameter was ~17.4 nm with a very wide pore size distribution. In fact, GO displays pore sizes in the range from 1 to 40 nm. However, MGO shows a much broader pore size distribution about 1 to 50 nm. Such vicissitudes in pore size distribution may be related to the effect of $Fe_3O_4$ in tailoring the pore structure of the nanocomposites. Also, for pure GO, the pore volume remained steady at ~0.32–0.33 cm$^3$ g$^{-1}$, whereas with $Fe_3O_4$ inducing pore volume decreased to ~0.23–0.24 cm$^3$ g$^{-1}$. The pore diameter analysis (Fig. S5) indicated that spacing in GO was large enough so metal ions can penetrate the interlayer of GO and could be adsorbed efficiently [44].

### 3.2. Experimental design of ultrasound-assisted adsorption

#### 3.2.1. Analysis of CCD

Optimization of DEP adsorption under RSM approach, based on four factors in five levels CCD and their subsequent analysis by linear, two-factor interactions (2FI), quadratic, and cubic models are listed in Table S2. The results indicate that the $R^2$ and Adjusted $R^2$ in the quadratic model greater than other models. In fact, software output indicated a quadratic model with $R^2$ > 0.95 and Lack of Fit p-value > 0.2 is fitted by experimental data. Therefore, the quadratic model gives usefully and suggestive information about the contribution of pH, adsorbent mass, time of sonication, and DEP concentration on the efficiency of the system. According to the RSM results supported with ANOVA analysis, the following model was constructed to express dependency of response function (Y) to independent variables (X$_s$):

Y (%)

$$= 72.658 - 15.25A + 6.5B + 4.62C - 9.00D - 8.5AB - 2.75$$
$$AC + 2.25AD - 0.5BC - 2.25BD + 0.75CD - 2.29013A$$
$$^2 + 0.834875B^2 - 1.03513C^2 - 0.915125D^2 \quad (8)$$

where Y is the DEP adsorption (%) and A. B. C and D denote the pH, adsorbent mass, sonication time and DEP concentration, respectively. The effects of adsorption process on various factors were demonstrated by Eq. (8). The negative and positive coefficient in the above equation describes antagonistic and synergistic effects on DEP adsorption [45]. It can be seen, B and C have a positive effect, while A and D have a negatively impact on the adsorption process. In reality, increased the adsorbent mass and sonication time is making an increase in adsorption efficiency and in contrary to increasing amounts of pH and DEP concentration, adsorption efficiency decreased. A (pH) in ANOVA test, and Eq. (8) possessed the highest coefficient, so can claim that this parameter has a significant effect on the adsorption process compare than another one.

The variance analysis was performed applying ANOVA for the validation study of models and the significance of variables (Table S3). The high value of models $R^2$ (0.997 were obtained for DEP adsorption) indicates that in all of the experiments, only < 0.23% of the total variations were not described by the quadratic model. The Model F-value of 188.80 strongly suggested that the model was significant. The chance of obtaining a very high F-value was found to be only 0.01%, which was possibly associated with the noise. Values of "Prob > F" < 0.05 indicated that model terms were significant. Also, the "Pred R-Squared" of 0.952 agreed with the "Adj R-Squared" of 0.992; i.e., the difference, which is < 0.2, confirms good correlations between the response and variables. The low values coefficient of variation (CV = 1.95) indicated a high degree of precision and a good deal of reliability of the experimental values. The "Lack of Fit F-value" of 2.41 implies the Lack of Fit is not significant relative to the pure error. There is a 20.55% chance that a "Lack of Fit F-value" this large could occur because of noise. Non-significant lack of fit indicating an appropriate model correlation between the variables and response. "Adeq Precision" measures the signal to noise ratio. A ratio > 4 is desirable. Adeq Precision ratio of 52.710 indicates an adequate signal. This model can be used to navigate the design space. The terms with "Prob > F" values > 0.05 were considered statistically insignificant (BC and CD). In term of interaction, the ANOVA test depicted AB, AC, AD, BD is significant, and the significant degree of quadratic factors followed the sequence: $A^2 > C^2 > D^2 > B^2$.

3D response surface plots were designed to identify the effect of variables individually and cumulatively as well as the interaction between these variables and the response. These plots (Fig. 1) were
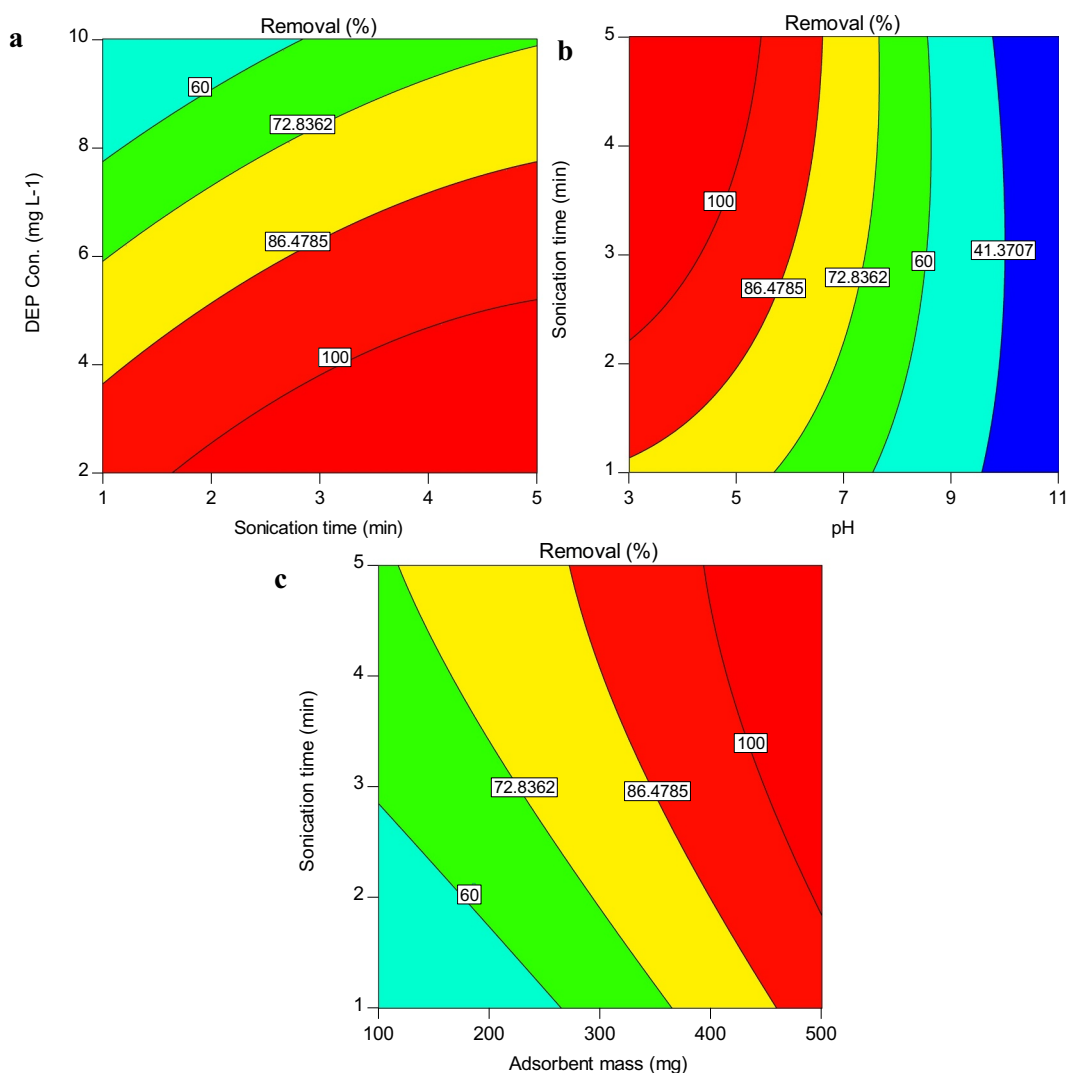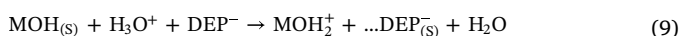


Fig. 1. Response surfaces for the CCD, the influence of interaction term between DEP concentration Vs. ultrasonic time (a), pH Vs. ultrasonic time (b) and adsorbent mass Vs. ultrasonic time (c) onto DEP adsorption.

acquired by varying two factors while maintaining the other constantly. The surface plot (Fig. 1a) reveals that at low DEP concentration and long sonication time, the adsorption efficiency was found to be high. It can be related to the issue that all adsorbents have limited active sites on self-surface, which may have become saturated at a specific concentration from adsorbate. Moreover, we recorded a significant increase in adsorption capacity at a short exposure time of sonication, which indicates a strong influence of ultrasound irradiation on mass transfer. The improvement of DEP sorption using ultra-sonication could also be resulted because of the shock waves with high-pressure characteristics and fast generation of micro-jets due to the presence of cavitation bubbles on the adsorbent-adsorbate interface. The effect of both pH and ultrasonic time on DEP adsorption (%) can be found in Fig. 1b. The adsorption efficiency was found to increase in acidic condition and showed a sharp decrease with a further rise in pH. This situation is due to the electrostatic attraction of DEP to the positive surface charge of MGO (Eq. (9)) or reaction of DEP with a surface group of the solid adsorbent (Eq. (10)) (pHzpc 7.85 ± 0.3). Moreover, the decrease in adsorption efficiency as pH increases (pH from 3 to 11) can be attributed to the decrease of positive surface charge density or ion exchange capacity of the solid.

$$MOH_{(S)} + H_3O^+ + DEP^- \rightarrow MOH_2^+ + \ldots DEP_{(S)}^- + H_2O \qquad (9)$$

$$MOH_{(S)} + H_3O^+ + DEP^- \rightarrow M^+ \ldots DEP_{(S)}^- + 2H_2O \qquad (10)$$

These equations can explain the change in DEP sorption mechanism with the increase of the equilibrium pH. However, the sorption reaction that occurs at pH > 7.85 may be described more efficiently by the following reaction (Eq. (11)).

$$M - OH_{(S)} + DEP_{(aq)}^- \rightarrow M^+ \ldots DEP_{(S)}^- + OH^- \qquad (11)$$
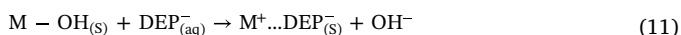
When pH > pHzpc, the surface of the solid becomes negative and, the DEP adsorption capacity consequently decreases because of the Coulomb repulsion of the same charges between the solute in a solution and the solid surface.

A similar trend of pH effect was observed for the adsorption of Diethyl phthalate on activated carbon [46], as well as for the adsorption of di-ethyl-phthalate on surfactant-coated nano/microsized alumina [47] and clay minerals [15].

Fig. 1c presents the interaction between adsorbent mass and exposure time of solution to ultrasound for the magnetic solid-phase adsorption of DEP. The adsorption of DEP was improved with an increase in the MGO dose and ultrasonic time which may be attributed to enlargement in the availability of adsorbent surface area with an increased number of adsorption sites accessible for DEP extraction. The rapid rates of DEP sorption in considerably reduced contact time may be due to enhancing availableness of adsorption sites ensuing from the ultrasound-mediated dispersion of adsorbent moieties in solution. In the study of Shaida et al. on DEP removal on mineral-rich waste coal modified with chitosan was reported that with increasing the absorbent dose from 10 to 40 mg/L, the efficiency increased from 11 to 91.1%, and time also had a direct relationship with DEP removal [48]. In a conducted study on ultrasound-assisted adsorption of dyes was observed that the removal efficiency was increased from 47 to 100% when the contact time increased from 5 to 50 min. They found the maximum removal of MG could be achieved at higher sonication time that suggests rapid uptake and quick establishment of equilibrium. The adsorption rate in low sonication time is very rapid due to the highly available adsorbent surface area and vacant sites achieved and enhanced by the dispersion of adsorbent into solution via ultrasonic power. And also, mass transfer due to raising diffusion coefficient encounter to enhance in adsorption rate [49]. Asfaram [50] and Li [51] in their studies reported similar results in dyes and heavy metals removal by ZnS: Mn-NPs-AC and Ca−Al hydrotalcite as adsorbent.

### 3.2.2. Analysis of AAN

In this work, ANN was applied in order to model DEP adsorption studies with experimental data using CCD operating conditions to train and test the neural network model. To determine the best ANN model, 1–20 of neurons were employed in the hidden layer. The relation MSE and number of neurons in the hidden layer were given in Table S4. Three common types of the learning algorithm, i.e., Levenberg-Marquardt (LM), Fletcher-Reeves (FR) conjugate gradient and scaled conjugate gradient were performed to select the most optimum algorithm that gives best back-propagation learning, as evident in Table S4, the ANN, which contains 5 hidden neurons based on the minimum MSE in the training, validation and testing datasets, was attained as the optimal structure of the ANN model for the adsorption of DEP by MGO [52]. In an optimum number of hidden layer neurons, the MSE for the training, validation and testing datasets was found 0.0019, 0.0008 and 0.0019, respectively, which indicates the LM algorithm with the minimum MSE and 5 artificial neurons in the hidden layer as the best back-propagation learning algorithm, consequently, best model for DEP adsorption.

The regression plots of the network outputs for training, validation, and test sets, as well as the network's efficiency through regression (R), are shown in Fig. S6. An ideal fit (network outputs exactly match the targets) would present $R = 0.996$. The results of this study show a good correlation among output values and targets during training ($R = 0.997$), validation ($R = 0.988$), and testing ($R = 0.99875$). The variation of the MSE for the various iterations of the optimum ANN model is shown in Fig. S7. As can be ascertained from Fig. S7, the errors associated with validation and testing presented a decreasing profile to the 4th iteration at the beginning of the training process. After the initial phase, the error within the validation set starts to rise, whereas it keeps decreasing in the training set. After 4 epochs increase, the validation error stopped continuous decrease and presented a slight increase together with test error since the training is stopped [53]. Table S5 shows the weight matrix and bias values of each selected layer. IW and b1 represent weight and bias of hidden layer, whereas LW and b2 are of output layers. The fitness function used for ANN models to correlate the inputs with the output is determined with the following equation:

$$ANN = Pureline \left( LW * tansig \left( IW * [x(1); x(2); x(3); x(4)] + b1 \right) + b2 \right) \qquad (12)$$

where the inputs are presented with x (from 1 to 4).

In order to determine the relative importance of input variables on DEP extraction, Garson equation (Eq. (8)) based on the weight matrix of the proposed optimized network have been used. ANN provided the weights for the coefficients between the artificial neurons (Table S5), which represent the interaction between axons and dendrites in biological systems, where each weight is responsible with the proportion of the incoming signal before transmitting to the whole body [34]. The relative importance of 4 input variables was calculated by Garson equation and shown in Fig. S8. According to Fig. S8, pH (X1), adsorbent dose (X2), sonication time (X3) and DEP concentration (X4) were calculated to be 32.74, 18.98, 39.37 and 8.91, respectively, which confirms the strong effect of each variable on DEP adsorption. The most and least effective variables were sonication time and DEP concentration, respectively.

### 3.2.3. Comparison of prediction abilities of RSM and ANN

The responses, which were obtained from the experimental data, were compared and then used to evaluate the prediction and modeling efficiency of ANN and RSM methods for DEP adsorption mechanism. Good applicability of prediction of the models was confirmed with $R^2$ values close to 1.0 with a small error function comparison of statistical parameters acquired from ANN and RSM is shown in Table 1. The RMSE values from RSM (3.435) and ANN (3.438) methods confirm that both prediction methods showed similar prediction for DEP adsorption

(%). Furthermore, the $R^2$ values of DEP adsorption were determined by RSM and ANN (see matrix of ANN-RSM from Fig. S9), and the AAD values of adsorption process (observed as 0.584 and 0.081%) revealed that both models provided good quality predictions for the experimental data with stable responses. Nevertheless, the ANN was found to show more accuracy in prediction compared to RSM.

The model-predicted values vs. residual values corresponding to the experimental data set are shown in Fig. S10a. The ANN and RSM models show an almost complete independence structure and random distribution over the [−1.65, 1.65] interval between residuals and predicted values of DEP adsorption efficiency. If the residuals appear to behave randomly, it suggests that the model fits the data well, otherwise, non-random pattern in the residuals, suggesting that the model not fit the data adequately. The sample of data associated with experimental runs against corresponding residual values for two models is shown in Fig. S10b. The RSM model exhibits greater deviation (variations) than the ANN model. In another side, the fluctuations of the residuals are relatively small and regular for the ANN model compared to the RSM model.

### 3.2.4. Comparison of optimization abilities of RSM and ANN

In CCD model, the optimization process (profile for predicted values and desirability option) was carried out to determine the optimum value of DEP adsorption efficiency, using the Design Expert software. According to the software optimization step, the desired goal for each operational variable (*initial pH (X1), DEP concentration (X2), adsorbent dose (X3) and sonication time (X4)*) was chosen in the studied range. The response (DEP adsorption efficiency) was defined as the maximum to achieve the highest performance. This procedure involves specifying the Desirability Function (DF) in the range of 0.0 (undesirable) to 1.0 (very desirable) for ultrasonic assisted simultaneous adsorption percentage of DEP by assigning predicted values (Table S6). The CCD optimization design matrix shows that the highest adsorption performance (99.378%) for DEP with the desirability of 1.0, was achieved under the following conditions: pH (4.912), adsorbent dose (0.333 g L$^{-1}$), ultrasonic time (3.457 min) and initial DEP concentration (5.124 mg/L). In another side, the developed ANN model was then used for optimization by the GA technique with the objective of maximization of DEP adsorption efficiency from aqueous solution. The values of GA specific parameters used in the optimization technique were as population size, crossover probability, and mutation probability

equal to 16, 0.9, and 0.01, respectively. Optimum situations have been selected after the assessment of GA for 59 iterations to achieved decent adsorption percentage of DEP (Fig. S11). The optimized conditions were obtained as follows: the pH of 5.38, adsorbent dose 334.708 mg/L, 4.241 mg/L of DEP concentration, and 3.723 min sonication. The extraction efficiency (%) of DEP under these optimized conditions was 100.55% using GA (Table S6).

To test the reliability of RSM and ANN optimization, five experiments ($N = 5$) was run under the obtained optimal conditions, and the adsorption efficiency was obtained as 96.822% ± 1.560 and 99.932% ± 0.091 for RSM and ANN models, respectively (Fig. 2). These outcomes affirmed the validity of the two models, however the experimental value was determined to be quite close to the predicted value (99.378%) in comparison with ANN result (100.55%), suggesting that empirical model got from ANN experimental design can be utilized to sufficiently describe the relationship between the independent variables and response. Besides, *t*-test at 95% confidence interval revel absence of significant difference between the test and ANN optimization response, which confirm the high efficiency of the model for best explanation and representation of information (data). The residual error between the ANN optimization response and test values were < 1.7%. This error affirms the validity of the developed ANN-GA model. The results obtained from the present study are consistent with the previous studies outcome by Mourabet [54] and Geyikçi [55]. They compared the RSM and ANN models in adsorption Fluoride and lead, respectively, and reported that The ANN model had been found to fit the data better and to have higher predictive capability than RSM.

### 3.3. Adsorption isotherm

Adsorption isotherms describe the relationship between the adsorbate and adsorbent, interaction mechanism, and maximum adsorption capacity of MGO. Herein, equilibrium studies performed by fitting the experimental data to Langmuir, Freundlich, Temkin, and Dubinin–Radushkevich isotherm models. Regression analysis ($R^2$) and error functions ($X^2$) was used to confirm the fitted model with measured data [35]. The isotherm constants for the adsorption of DEP onto MGO are given in Table 2. As seen, the highest correlation coefficients ($R^2 > 0.993$) and lowest error function (0.014) is owned by the Langmuir model. This result reveals that the Langmuir model is well appropriate to describe the DEP adsorption process on MGO, compared

**Table 1**
Comparison of statistical parameters obtained using the ANN and RSM.

| | Prediction abilities | | | Optimization abilities | |
|---|---|---|---|---|---|
| | Actual | RSM | ANN | Repeat E CCD | Repeat E ANN |
| N total | 21 | 21 | 21 | 5 | 5 |
| Standard deviation | 15.759 | 15.741 | 15.755 | 1.560 | 0.091 |
| RMSE | 3.439 | 3.435 | 3.438 | 0.187 | 0.040 |
| MAE | 0.003 | 0.027 | 0.008 | 0.018 | 0.002 |
| AAD | 0.0732 | 0.584 | 0.081 | 0.260 | 0.040 |
| Variance | 248.369 | 247.806 | 248.246 | 2.435 | 0.008 |
| Uncorrected sum of squares | 108,053.7 | 108,042.4 | 107,985.1 | 46,882.434 | 49,932.056 |
| Corrected sum of squares | 4967.382 | 4956.132 | 4964.933 | 9.742 | 0.033 |
| Coefficient of variation | 0.224 | 0.224 | 0.224 | 0.016 | 9.16E−04 |
| Mean absolute deviation | 12.425 | 12.307 | 12.413 | 1.201 | 0.073 |
| SD times 2 | 31.519 | 31.483 | 31.511 | 3.121 | 0.182 |
| SD times 3 | 47.279 | 47.225 | 47.267 | 4.681 | 0.274 |
| Geometric mean | 68.137 | 68.143 | 68.116 | 96.812 | 99.931 |
| Geometric SD | 1.287 | 1.287 | 1.287 | 1.016 | 1.000 |
| Minimum | 33 | 32.997 | 33.000 | 94.54 | 99.79 |
| 1st quartile (Q1) | 61 | 60.382 | 61.000 | 96.1 | 99.89 |
| 3rd quartile (Q3) | 79 | 78.382 | 79.000 | 98.15 | 100 |
| Maximum | 94 | 93.997 | 94 | 98.31 | 100 |
| P90 | 89 | 88.997 | 89.000 | 98.31 | 100 |
| P95 | 93 | 93.622 | 93.081 | 98.31 | 100 |
| P99 | 94 | 93.997 | 94 | 98.31 | 100 |
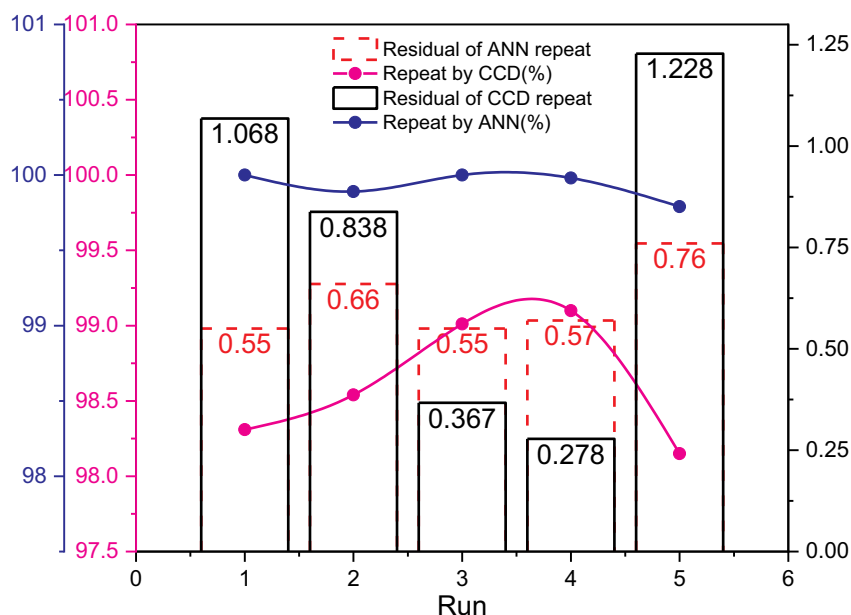
**Fig. 2.** Plot of the optimization and residuals of five experiments ($N = 5$) versus model optimization values.

to Freundlich, Temkin, and D-R isotherms (see Fig. S12a). Langmuir model suggests that active sites were distributed homogeneous form on the adsorbent surface and adsorption of DEP on MGO take place in a monolayer adsorption manner. Depending on the value of $R_L$, the adsorption process could be evaluated as irreversible ($R_L = 0$), favorable ($0 < R_L < 1$), linear ($R_L = 1$) and unfavorable ($R_L > 1$) [56]. The dimensionless parameter of $R_L$, constant separation factor, which derived from the Langmuir model, was calculated using the following equation:

$$R_L = \frac{1}{1 + K_L C_0} \tag{13}$$

From Table 2, the values of $1/n$ as the adsorption intensity factor or surface heterogeneity were found in the range between 0 and 1, while the values of $R_L$ for DEP were obtained to be in the ranges 0.023–0.367, which strongly indicates that the adsorption of DEP onto MGO is favorable. The values of the mean adsorption energy, E, can be used to predict the physical and chemical nature of extraction. The magnitude of $E < 8\,kJ\,mol^{-1}$ indicates that the adsorption process is of physical nature, $E = 8$–$16\,kJ\,mol^{-1}$ (ion exchange) and chemical adsorption takes place when the value of E bigger than $20\,kJ\,mol^{-1}$. The value of E for DEP adsorption onto MGO determined by the D-R model was found to be $> 8\,kJ\,mol^{-1}$, indicating that the adsorption of DEP onto the adsorbent is a chemisorption mechanism.

### 3.4. Comparison of this method and adsorbent with other literature

The comparison of contact time and maximum sorption capacity ($q_{max}$ calculated from the Langmuir isotherm model) for the adsorption of DEP on various nanomaterial sorbents in single and binary systems is summarized in Table 3. It was observed that the $q_{max}$ of MGO nanocomposite in the presence of the US for DEP adsorption was found to be $136.840\,mg/\,g$, which are higher than that for other adsorption systems reported. On the other hand, better adsorption capacity in the present system in comparison to other adsorbents can clearly show the role of ultrasound in wastewater treatment.

### 3.5. Adsorption kinetic and comparison of adsorption + stirring Vs. adsorption + ultrasound

To investigate the mass transfer rate and mechanism of ultrasound-assisted simultaneous adsorption of the DEP process, the experimental data are fit and correlated with pseudo-first- and second-order kinetic models, Elovich, and intraparticle diffusion. The kinetic parameters for each model at the optimized condition of ANN are given in Table 2 and Fig. S12b. The higher value of correlation coefficient ($R^2 > 0.997$) and the low difference between $q_{e\_exp}$ (experimental) and $q_{e\_cal}$ (calculated) indicate the high ability of the pseudo-second-order model for the demonstration of experimental data. To identify the diffusion mechanism, the kinetic results were then subjected to analysis by intraparticle diffusion model based on the Weber and Morris theory. The $C = 0$ (Morris theory reveals that the regression of $q_t$ versus $t^{1/2}$ is linear with the intercept C), indicates that the adsorption process just controlled by intraparticle diffusion. Here, the deviation of straight lines from the non-zero C value (figure not shown) was observed suggesting that the pore diffusion is not the lone rate-controlling stage and adsorption conforms from intraparticle diffusion + pseudo-second order, kinetic model. The values of C explained the thickness of the boundary layer. The larger the intercept (larger C value), the greater is the boundary layer effect.

After determination the best kinetic model, effect of presence or absence ultrasound and changes its frequency on the DEP adsorption capacity and rate constant was investigated using the pseudo-second-order kinetic model. The results show that the hybrid adsorption + ultrasound process had better performance than the adsorption + stirring system. Analysis of the kinetic data indicates that DEP adsorption rate ($k_2$) and its capacity ($q_e$) in the presence of ultrasound with 35 kHz ($q_e = 38.696$, $k_2 = 0.159$, $R^2 = 0.997$) in comparison with the adsorption rate obtained without ultrasound ($q_e = 12.742$, $k_2 = 0.043$, $R^2 = 0.924$) and smaller intensity ($q_e = 29.570$, $k_2 = 0.085$, $R^2 = 0.989$) significantly increased (see Table 2, $C_0 = 4.21$). An increase the kinetic rate constant in the presence of ultrasound and its improvement by growing the ultrasound frequency showed that shorter time is required to uptake and separate the same amount of pollutants as compared to the adsorption + stirring system. These results clearly reveal that ultrasound plays an important role in improving DEP adsorption. Improvement of adsorption capacity may be due to that this process creates acoustic cavitation, which leads to the collapse of bubbles at small time periods and results in consequent pressure and local heating. This situation may accelerate overall mass transfer and kinetic rate.

**Table 2**

Isotherm, kinetic and thermodynamic constant parameters and correlation coefficients calculated for the DEP adsorption onto MGO adsorbents under ANN optimized condition.

| Model | Equation | Nomenclature | Parameters | DEP | |
|---|---|---|---|---|---|
| | | | | Values | $X^2$ |
| **Isotherms** | | | | | |
| Langmuir | $C_e/q_e = C_e/Q_m + 1/K_a Q_m$ | The slope and intercept of the linear plot of $C_e/q_e$ versus $C_e$ give $Q_m$ and $K_a$, respectively. | $Q_m$ (mg/g)<br>$K_L$ (L mg$^{-1}$)<br>$R_L$<br>$R^2$ | 116.933<br>0.689<br>0.993<br>0.024–0.367 | 0.014 |
| Freundlich | $\ln q_e = (1/n)\ln C_e + \ln K_F$ | The slope and intercept of the linear plot of $\ln q_e$ versus $\ln C_e$ give $1/n$ and $K_F$, respectively. | $n$<br>$K_F$ (L mg$^{-1}$)<br>$R^2$ | 6.545<br>59.642<br>0.968 | 0.035 |
| Temkin | $q_e = B_l \ln C_e + B_l \ln K_T$ | $B_l$ and $K_T$ are calculated from the slope and intercept of the linear plot of $q_e$ against $\ln C_e$, respectively. | $B_l$<br>$K_T$ (L mg$^{-1}$)<br>$R^2$ | 7.851<br>8294.209<br>0.845 | 0.024 |
| Dubinin and Radushkevich | $\ln q_e = -K\varepsilon^2 + \ln Q_s$,<br>$(\varepsilon = RT \ln (1 + 1/C_e))$ | The slope and intercept of the linear plot of $\ln q_e$ versus $\varepsilon^2$ give $K$ and $Q_s$, respectively. | $E$ (kJ mol$^{-1}$)<br>$D$ (mol$^{-2}$ kJ$^{-2}$)<br>$R^2$ | 814.318<br>3.582E−09<br>0.693 | 0.034 |
| **Kinetics** | | | | | |
| First-order kinetic | $\ln(q_e - q_t) = -k_1 t + \ln(q_e)$ | The slope and intercept of the linear plot of $\ln(q_e - q_t)$ versus $t$ give $k_1$ and $q_e$, respectively. | $k_1$ (min$^{-1}$)<br>$q_e$ (mg/g)<br>$R^2$ | 0.027681698<br>43.82503491<br>0.9708 | 0.0259 |
| Second-order kinetic | $t/q_t = t/q_e + 1/(k_2 q_e)^2$ | The slope and intercept of linear plot of $t/q_t$ versus $t$ give $q_e$ and $k_2$, respectively. | $k_2$ (g mg$^{-1}$ min-1)<br>$q_e$ (mg/g)<br>$R^2$ | 0.1591201<br>38.69627679<br>0.9971 | 0.0152 |
| Intraparticle diffusion | $q_t = K_{diff} t^{1/2} + C$ | The slope and intercept of the linear plot of $q_t$ versus $t^{1/2}$ give $K_{diff}$ and $C$, respectively. | $K_{dif}$ (g mg$^{-1}$ min-0.5)<br>$C$<br>$R^2$ | 2.161943699<br>0.012548478<br>0.9196 | 0.0353 |
| Elovich | $q_t = 1/\beta \ln(t) + 1/\beta \ln(\alpha\beta)$ | $\beta$ and $\alpha$ are obtained from the slope and intercept of the plot of $q_t$ versus $\ln (t)$, respectively. | $\beta$ (g mg$^{-1}$)<br>$\alpha$ (g mg$^{-1}$ min$^{-1}$)<br>$R^2$ | 8.544725932<br>0.026101738<br>0.9876 | 0.0643 |
| $q_e(exp) = 36.417$ for $C_0 = 4.21$ mg/L | | | | | |
| Pseudo-second-order kinetic models | Under stirring (at 150 rpm) | | $k_2$ (g mg$^{-1}$ min-1)<br>$q_e$ (mg/g)<br>$R^2$ | 0.043<br>12.742<br>0.924 | 0.025 |
| | US-15 kHz | | $k_2$ (g mg$^{-1}$ min-1)<br>$q_e$ (mg/g)<br>$R^2$ | 0.085<br>29.570<br>0.989 | 0.023 |
| | US-35 kHz | | $k_2$ (g mg$^{-1}$ min-1)<br>$q_e$ (mg/g)<br>$R^2$ | 0.159<br>38.696<br>0.997 | 0.015 |

| Thermodynamic for $C_0 = 6$ mg/L | | | | | |
|---|---|---|---|---|---|
| Temperature (K) | $\ln k_d$ | $\Delta S°$ (kJ mol$^{-1}$·K) | $\Delta G°$ (kJ mol$^{-1}$) | $\Delta H°$ (kJ mol$^{-1}$) | R % |
| 293 | 4.527 | 0.223 | −11.029 | 791.026 | 92.53 |
| 308 | 5.326 | | −13.640 | | 96.5 |
| 323 | 6.622 | | −17.782 | | 99.01 |

## 3.6. Adsorption thermodynamics

Influence of temperature on ultrasound-assisted simultaneous adsorption of DEP (%) was examined above the range of 293–308 K and has been displayed in Table 2. The results showed that a sharp increase in the adsorption capacity of DEP occurred when the temperature of the solutions raised from 293 to 308 K and a higher temperature is favored by adsorption process. Increase temperature with a possible impact on total pore capacity and porosity of adsorbent led to increaseing diffusion of DEP molecules above the external surface in addition to inner pores of MGO. The increase in aqueous solutions temperature also facilitated a higher number of cavitation bubbles formed in the liquid bulk and improved dispersion of MGO thereby; thereby accelerate the DEP adsorption rate. For better understanding, the thermodynamic parameters of DEP adsorption process were conducted at three temperatures of 298, 303, and 308 K and summarized in Table 2. The distribution coefficient constant ($K_d$) used for determining the thermodynamic parameters and the slope and intercept of the Van't Hoff plot ($\ln K_d$ versus $1/T$) is used for calculating the numerical values of $\Delta H°$ and $\Delta S°$. The values of $\Delta G°$ are negative and indicate a spontaneous

**Table 3**

Comparison of adsorption capacity of DEP between various adsorbents found in the literature.

| Adsorbent | Phthalate ester | pH | Isotherm | Kinetic | $q_m$ (mg/g) | References |
|---|---|---|---|---|---|---|
| MZNC | DMP | 3.0 | Langmuir | Pseudo-second order | 109.52 | [57] |
| Chitosan bead | DHpP | 8.0 | Freundlich | Pseudo-second order | 1.52 | [58] |
| Poly(EGDMA-MATrp) beads | DEP | 5.0 | Langmuir | Pseudo-second order | 59.7 | [59] |
| Magnetic iron–carbo composite | DEP | 4.0 | Langmuir | Pseudo-second order | 120.54 | [60] |
| Magnetic graphene oxide | DEP | 3.0 | Langmuir | Pseudo-first order | 8.71 | [40] |
| Phoenix leaves activated carbon | DBP | 3.0 | Freundlich | Pseudo-second order | 48.68 | [61] |
| MGO-US | DEP | 5.38 | Langmuir | Pseudo-second order | 116.933 | This work |

adsorption process. The positive value of ΔH° indicates that adsorption of the DEP on MGO is endothermic. Besides, the type of sorption process can be explained in terms of ΔH°. Generally, the ΔH° values between 2.1 and 20.9 KJ/mol and 80–200 KJ/mol revealed that the process is physisorption and chemosorption, respectively. The positivity and the magnitude of ΔH° values obtained for the adsorption of DEP (ΔH° = 791.026) suggest a chemosorption process. The value of ΔS° is calculated as $0.223\,kJ\,mol^{-1}$, The positive ΔS° illustrates increased randomness at the solid-liquid interface during the adsorption process, as the target molecules are fixed to the two-dimensional surface from the solution.

### 3.7. Regeneration and reusability

The reusability of MGO composite as an effective adsorbent for DEP removal was studied in ten consecutive cycles. The regeneration of used adsorbent was studied by with methanol at 45 °C followed by washing with de-ionized water for the regeneration of active sites for binding during 40 min under optimized condition. In the first cycle, DEP removed completely. However, the efficiency of adsorption and desorption reduced to 75.0 and 73.0% respectively in the 10th cycle (Fig. S12c). It confirmed the stability and the feasibility of the prepared magnetic adsorbent that can be regenerated and reused without compromising on the adsorption capacity up to ten cycles at least.

### 3.8. Simulated DEP removal from wastewater and adsorption mechanism

The applicability of hybrid adsorption + ultrasound system (US-MGO) was validated by removing DEP from actual wastewater and spiked with 5 and 15 mg/L DEP. The wastewater samples were collected from municipal drainage with the specifications given in Table S7. The chemical oxygen demand (COD) of the collected wastewater, wastewater spiked with 5 mg/L DEP and wastewater spiked with 15 mg/L DEP were measured to be 50, 72 and 126 mg/L. The increase in the COD was clearly due to the addition of DEP to the wastewater contents. The DEP spiked wastewater was treated under the optimized condition, and the concentration of the DEP and its COD in the residual was determined by HPLC. The HPLC chromatogram presented that the residual of DEP concentration after treatment was reduced by 80% for $C_0 = 5$ mg/L and 61% for $C_0 = 15$ of DEP and their corresponding COD was 21 and 39.76 mg/L, respectively. While in lower concentrations, i.e., 0.5, 1, 2.5 and 4 mg/L, the higher removal efficiency was observed ($R > 87.34\%$) (Fig. S12d and e and its calibration curve is shown in Fig. S13). This evidence suggests that lower concentrations will be eliminated better under hybrid adsorption + ultrasound system (US-MGO) from municipal wastewater matrix, which will be desirable. In general, the decrease in DEP adsorption efficiency can be due to the presence of TDS, various ions and/or organic compound and impurities that present in the real wastewater.

The adsorption mechanisms of DEP on MGO are dependent on the adsorbate-adsorbate, adsorbate-solvent which largely depend on physical, chemical, and electrostatic interaction. The π-π interaction, hydrophobic effect, hydrogen bonding, and electrostatic interaction are commonly used to demonstrate the adsorption mechanism of DEP on MGO (see Fig. S14). Suitable surface area and high pore volume of MGO can reduce the diffusion resistance and adsorption energy, making DEP transport easier as well. However, the main and effective mechanism in the DEP adsorption process can be considered as follows: (a) π-π electron donor-acceptor (EDA) can be a primary adsorption enhancement mechanism for DEP with strong π-electron donating ability or strong π-withdrawing ability, due to the interaction of DEP molecule with π region of graphene oxide surface. In fact, the adsorption affinity for DEP could be due to the π-π EDA interaction of aromatic structure (benzene ring) of DEP with magnetic graphene oxide. (b) a lot of hydroxyls group on MGO can directly formation of a hydrogen bond with the oxygen atom of the ester group of DEP, promoting the DEP to approach to

MGO. (c) Solution pH influences the surface charge of the adsorbent and the dissociation level of the organic compounds. At pH < pHpzc (5.38 < 7.85 for the present study), various functional groups in MGO are protonated and resulted in a positively charged surface of MGO. Subsequently, electrostatic attraction is established between negatively charged of DEP (due to carboxylic and phenolic functional groups and …) and positive charge present on the surface of MGO, which increases the efficiency.

## 4. Conclusions

A multi-response optimization study based on CCD allows searching optimum conditions to achieve the best and maximum DEP adsorption onto MGO by the aid of ultrasound. Values of "Prob > F" < 0.0001 indicate model terms have a significant effect on adsorption of DEP. Maximum DEP removal (percentage ~100% and sorption capacity = 116.933 mg/g) was obtained at pH 5.38, 0.334 g adsorbent mass, $4.241\,mg\,L^{-1}$ of DEP at 3.723 min sonication. The ANOVA results enunciated that the significance of the parameters is as follows (the most to the least significant): pH > initial DEP concentrations > adsorbent mass > sonication time. Adsorption kinetics, including the pseudo-first-order, pseudo-second-order, Elovich, and intraparticle diffusion models were researched, and the data fitted better with the pseudo-second-order kinetic model ($R2 = 0.997$). For adsorption isotherms, Langmuir isotherm was proved to be the best correlation ($R2 = 0.993$) compared with the Freundlich, Temkin, and Dubinin–Radushkevich models. The positive value of ΔH° and negative value of ΔG° also indicates that DEP adsorption process is spontaneous and endothermic. A kinetic study revealed that the $q_{max}$ and $k_2$ parameter were significantly improved under sonication conditions. This confirmed that sonication enhances the kinetics of adsorption via cavitation formation generated by acoustic energy. The real application of US-MGO system has been demonstrated here by successfully treating repeatedly municipal wastewater spiked with DEP.

## Author contribution

All authors have read the manuscript and agreed to submit it in its current form for consideration for publication in the journal.

## Declaration of competing interest

None.

## Acknowledgment

## Appendix A. Supplementary data

Supplementary data to this article can be found online at https://doi.org/10.1016/j.microc.2019.104144.

## References

[1] J. Fawell, C.N. Ong, Emerging contaminants and the implications for drinking water, Int. J. Water Resour. Dev. 28 (2012) 247–263.

[2] S. Yan, S.B. Subramanian, R. Tyagi, R.Y. Surampalli, T.C. Zhang, Emerging Contaminants of Environmental Concern: Source, Transport, Fate, and Treatment, Practice Periodical of Hazardous, Toxic, and Radioactive Waste Management, 14 (2009), pp. 2–20.

[3] A. Kiani, M. Ahmadloo, N. Shariatifar, M. Moazzen, A.N. Baghani, G.J. Khaniki, A. Taghinezhad, A. Kouhpayeh, A.M. Khanegheh, P. Ghajarbeygi, Method development for determination of migrated phthalate acid esters from polyethylene terephthalate (PET) packaging into traditional Iranian drinking beverage (Doogh) samples: a novel approach of MSPE-GC/MS technique, Environ. Sci. Pollut. Res. 25

(2018) 12728–12738.

[4] M. Moazzen, A.M. Khaneghah, N. Shariatifar, M. Ahmadloo, I. Eş, A.N. Baghani, S. Yousefinejad, M. Alimohammadi, A. Azari, S. Dobaradaran, Multi-walled carbon nanotubes modified with iron oxide and silver nanoparticles (MWCNT-Fe3O4/Ag) as a novel adsorbent for determining PAEs in carbonated soft drinks using magnetic SPE-GC/MS method, Arab. J. Chem. 12 (2019) 476–488.

[5] M. Zhang, Y. Cong, Y. Sheng, B. Liu, A direct competitive enzyme-linked im-munosorbent assay by antibody coated for diethyl phthalate analysis, Anal. Biochem. 406 (2010) 24–28.

[6] M. Wittassek, H.M. Koch, J. Angerer, T. Brüning, Assessing exposure to phthala-tes–the human biomonitoring approach, Mol. Nutr. Food Res. 55 (2011) 7–31.

[7] S. Net, R. Sempere, A. Delmont, A. Paluselli, B. Ouddane, Occurrence, fate, behavior and ecotoxicological state of phthalates in different environmental matrices, Environ. Sci. Technol. 49 (2015) 4019–4035.

[8] M. Gavrilescu, K. Demnerová, J. Aamand, S. Agathos, F. Fava, Emerging pollutants in the environment: present and future challenges in biomonitoring, ecological risks and bioremediation, New Biotechnol. 32 (2015) 147–156.

[9] E. Ahmadi, M. Gholami, M. Farzadkia, R. Nabizadeh, A. Azari, Study of moving bed biofilm reactor in diethyl phthalate and diallyl phthalate removal from synthetic wastewater, Bioresour. Technol. 183 (2015) 129–135.

[10] C.-H. Hung, C. Yuan, H.-W. Li, Photodegradation of diethyl phthalate with PANi/ CNT/TiO2 immobilized on glass plate irradiated with visible light and simulated sunlight—effect of synthesized method and pH, J. Hazard. Mater. 322 (2017) 243–253.

[11] T. Wang, T. Liu, Pulse electro-coagulation application in treating dibutyl phthalate wastewater, Water Sci. Technol. 76 (2017) 1124–1131.

[12] D.-W. Gao, Z.-D. Wen, Phthalate esters in the environment: a critical review of their occurrence, biodegradation, and removal during wastewater treatment processes, Sci. Total Environ. 541 (2016) 986–1001.

[13] C.P. Okoli, G.O. Adewuyi, Q. Zhang, P.N. Diagboya, Q. Guo, Mechanism of dialkyl phthalates removal from aqueous solution using γ-cyclodextrin and starch based polyurethane polymer adsorbents, Carbohydr. Polym. 114 (2014) 440–449.

[14] N.A. Khan, B.K. Jung, Z. Hasan, S.H. Jhung, Adsorption and removal of phthalic acid and diethyl phthalate from water with zeolitic imidazolate and metal–organic frameworks, J. Hazard. Mater. 282 (2015) 194–200.

[15] Y. Wu, Y. Si, D. Zhou, J. Gao, Adsorption of diethyl phthalate ester to clay minerals, Chemosphere 119 (2015) 690–696.

[16] Q. Chen, J. Zheng, Q. Yang, Z. Dang, L. Zhang, Effect of carbon chain structure on the phthalic acid esters (PAEs) adsorption mechanism by mesoporous cellulose biochar, Chem. Eng. J. 362 (2019) 383–391.

[17] Y. Wang, Y. Tong, X. Xu, L. Zhang, Developed magnetic multiporous 3D N-Co@ C/ HCF as efficient sorbent for the extraction of five trace phthalate esters, Anal. Chim. Acta 1054 (2019) 176–183.

[18] L. Gao, Y. Tang, C. Wang, L. Yao, J. Zhang, R. Gao, X. Tang, T. Chong, H. Zhang, Highly-efficient amphiphilic magnetic nanocomposites based on a simple sol-gel modification for adsorption of phthalate esters, J. Colloid Interface Sci. 552 (2019) 142–152.

[19] S. Kumar, C. Terashima, A. Fujishima, V. Krishnan, S. Pitchaimuthu, Photocatalytic Degradation of Organic Pollutants in Water Using Graphene Oxide Composite, a New Generation Material Graphene: Applications in Water Technology, Springer, 2019, pp. 413–438.

[20] Z. Geng, Y. Lin, X. Yu, Q. Shen, L. Ma, Z. Li, N. Pan, X. Wang, Highly efficient dye adsorption and removal: a functional hybrid of reduced graphene oxide–Fe3O4 nanoparticles as an easily regenerative adsorbent, J. Mater. Chem. 22 (2012) 3527–3535.

[21] X. Xu, J. Zou, X.-R. Zhao, X.-Y. Jiang, F.-P. Jiao, J.-G. Yu, Q. Liu, J. Teng, Facile assembly of three-dimensional cylindrical egg white embedded graphene oxide composite with good reusability for aqueous adsorption of rare earth elements, Colloids Surf. A Physicochem. Eng. Asp. 570 (2019) 127–140.

[22] L. Lu, J. Wang, B. Chen, Adsorption and desorption of phthalic acid esters on gra-phene oxide and reduced graphene oxide as affected by humic acid, Environ. Pollut. 232 (2018) 505–511.

[23] X.-R. Zhao, X. Xu, J. Teng, N. Zhou, Z. Zhou, X.-Y. Jiang, F.-P. Jiao, J.-G. Yu, Three-dimensional porous graphene oxide-maize amylopectin composites with con-trollable pore-sizes and good adsorption-desorption properties: facile fabrication and reutilization, and the adsorption mechanism, Ecotoxicol. Environ. Saf. 176 (2019) 11–19.

[24] S. Dashamiri, M. Ghaedi, A. Asfaram, F. Zare, S. Wang, Multi-response optimization of ultrasound assisted competitive adsorption of dyes onto Cu(OH)2-nanoparticle loaded activated carbon: central composite design, Ultrason. Sonochem. 34 (2017) 343–353.

[25] M.E. Gorji, R. Ahmadkhaniha, M. Moazzen, M. Yunesian, A. Azari, N. Rastkari, Polycyclic aromatic hydrocarbons in Iranian kebabs, Food Control 60 (2016) 57–63.

[26] F.C. Sampaio, T.L. da Conceição Saraiva, G.D. e Silva, J.T. de Faria, C.G. Pitangui, B. Aliakbarian, P. Perego, A. Converti, Batch growth of Kluyveromyces lactis cells from deproteinized whey: response surface methodology versus artificial neural network—genetic algorithm approach, Biochem. Eng. J. 109 (2016) 305–311.

[27] M. Baziar, A. Azari, M. Karimaei, V.K. Gupta, S. Agarwal, K. Sharafi, M. Maroosi, N. Shariatifar, S. Dobaradaran, MWCNT-Fe3O4 as a superior adsorbent for micro-cystins LR removal: investigation on the magnetic adsorption separation, artificial neural network modeling, and genetic algorithm optimization, J. Mol. Liq. 241 (2017) 102–113.

[28] E.E. Ghadim, F. Manouchehri, G. Soleimani, H. Hosseini, S. Kimiagar, S. Nafisi, Adsorption properties of tetracycline onto graphene oxide: equilibrium, kinetic and thermodynamic studies, PLoS One 8 (2013) e79254.

[29] L. Wang, N. Boussetta, N. Lebovka, E. Vorobiev, Ultrasound assisted purification of polyphenols of apple skins by adsorption/desorption procedure, Ultrason. Sonochem. 55 (2019) 18–24.

[30] R. Zare-Dorabei, S.M. Ferdowsi, A. Barzin, A. Tadjarodi, Highly efficient simulta-neous ultrasonic-assisted adsorption of Pb(II), Cd(II), Ni(II) and Cu(II) ions from aqueous solutions by graphene oxide modified with 2,2′-dipyridylamine: central composite design optimization, Ultrason. Sonochem. 32 (2016) 265–276.

[31] W. Zhang, Y. Liang, J. Wang, Y. Zhang, Z. Gao, Y. Yang, K. Yang, Ultrasound-as-sisted adsorption of Congo red from aqueous solution using MgAlCO3 layered double hydroxide, Appl. Clay Sci. 174 (2019) 100–109.

[32] R. Rezaee, A. Maleki, A. Jafari, S. Mazloomi, Y. Zandsalimi, A.H. Mahvi, Application of response surface methodology for optimization of natural organic matter degradation by UV/H2O2 advanced oxidation process, J. Environ. Health Sci. Eng. 12 (2014) 67.

[33] A. Esrafili, R. Rezaei Kalantary, A. Azari, E. Ahmadi, M. Gholami, Removal of diethyl phthalate from aqueous solution using persulfate-based (UV/Na2S2O8/ Fe2+) advanced oxidation process, Journal of Mazandaran University of Medical Sciences 25 (2016) 122–135.

[34] M. Kassaee, E. Motamedi, M. Majdi, Magnetic Fe3O4-graphene oxide/polystyrene: fabrication and characterization of a promising nanocomposite, Chem. Eng. J. 172 (2011) 540–549.

[35] J. Li, X. Wang, H. Duan, Y. Wang, Y. Bu, C. Luo, Based on magnetic graphene oxide highly sensitive and selective imprinted sensor for determination of sunset yellow, Talanta 147 (2016) 169–176.

[36] M. Gao, Z. Wang, C. Yang, J. Ning, Z. Zhou, G. Li, Novel magnetic graphene oxide decorated with persimmon tannins for efficient adsorption of malachite green from aqueous solutions, Colloids Surf. A Physicochem. Eng. Asp. 566 (2019) 48–57.

[37] G. He, W. Liu, X. Sun, Q. Chen, X. Wang, H. Chen, Fe3O4@ graphene oxide com-posite: a magnetically separable and efficient catalyst for the reduction of nitroar-enes, Mater. Res. Bull. 48 (2013) 1885–1890.

[38] A. Azari, R.R. Kalantary, G. Ghanizadeh, B. Kakavandi, M. Farzadkia, E. Ahmadi, Iron–silver oxide nanoadsorbent synthesized by co-precipitation process for fluoride removal from aqueous solution and its adsorption mechanism, RSC Adv. 5 (2015) 87377–87391.

[39] Z. Ma, Y. Guan, H. Liu, Synthesis and characterization of micron-sized mono-disperse superparamagnetic polymer particles with amino groups, J. Polym. Sci. A Polym. Chem. 43 (2005) 3433–3439.

[40] L. Yin, Y. Lin, L. Jia, Graphene oxide functionalized magnetic nanoparticles as adsorbents for removal of phthalate esters, Microchim. Acta 181 (2014) 957–965.

[41] Y. Zhang, B. Chen, L. Zhang, J. Huang, F. Chen, Z. Yang, J. Yao, Z. Zhang, Controlled assembly of Fe3O4 magnetic nanoparticles on graphene oxide, Nanoscale 3 (2011) 1446–1450.

[42] H.P. Cong, J.J. He, Y. Lu, S.H. Yu, Water-soluble magnetic-functionalized reduced graphene oxide sheets: in situ synthesis and magnetic resonance imaging applica-tions, Small 6 (2010) 169–173.

[43] M. Verma, A.P. Singh, P. Sambyal, B.P. Singh, S. Dhawan, V. Choudhary, Barium ferrite decorated reduced graphene oxide nanocomposite for effective electro-magnetic interference shielding, Phys. Chem. Chem. Phys. 17 (2015) 1610–1618.

[44] L. Fan, C. Luo, M. Sun, H. Qiu, Synthesis of graphene oxide decorated with magnetic cyclodextrin for fast chromium removal, J. Mater. Chem. 22 (2012) 24577–24583.

[45] A. Azari, B. Kakavandi, R.R. Kalantary, E. Ahmadi, M. Gholami, Z. Torkshavand, M. Azizi, Rapid and efficient magnetically removal of heavy metals by magnetite-activated carbon composite: a statistical design approach, J. Porous. Mater. 22 (2015) 1083–1096.

[46] S. Venkata Mohan, S. Shailaja, M. Rama Krishna, P.N. Sarma, Adsorptive removal of phthalate ester (di-ethyl phthalate) from aqueous phase by activated carbon: a ki-netic study, J. Hazard. Mater. 146 (2007) 278–282.

[47] J. Li, Y. Shi, Y. Cai, S. Mou, G. Jiang, Adsorption of di-ethyl-phthalate from aqueous solutions with surfactant-coated nano/microsized alumina, Chem. Eng. J. 140 (2008) 214–220.

[48] M.A. Shaida, R.K. Dutta, A.K. Sen, Removal of diethyl phthalate via adsorption on mineral rich waste coal modified with chitosan, J. Mol. Liq. 261 (2018) 271–282.

[49] M. Dastkhoon, M. Ghaedi, A. Asfaram, A. Goudarzi, S.M. Langroodi, I. Tyagi, S. Agarwal, V.K. Gupta, Ultrasound assisted adsorption of malachite green dye onto ZnS:Cu-NP-AC: equilibrium isotherms and kinetic studies – response surface opti-mization, Sep. Purif. Technol. 156 (2015) 780–788.

[50] A. Asfaram, M. Ghaedi, F. Yousefi, M. Dastkhoon, Experimental design and mod-eling of ultrasound assisted simultaneous adsorption of cationic dyes onto ZnS: Mn-NPs-AC from binary mixture, Ultrason. Sonochem. 33 (2016) 77–89.

[51] Y. Li, J. Wang, Z. Li, Q. Liu, J. Liu, L. Liu, X. Zhang, J. Yu, Ultrasound assisted synthesis of Ca–Al hydrotalcite for U (VI) and Cr (VI) adsorption, Chem. Eng. J. 218 (2013) 295–302.

[52] A. Maleki, H. Daraei, L. Alaei, L. Abasi, A. Izadi, Dye removal probing by electro-coagulation process: modeling by MLR and ANN methods, J. Chem. Soc. Pak. (2012) 34.

[53] F. Nasri, H. Daraei, T. Hatami, A. Maleki, Phase equilibrium of binary system carbon dioxide-methanol at high pressure using artificial neural network, J. Chem. Soc. Pak. (2012) 34.

[54] M. Mourabet, A. El Rhilassi, M. Bennani-Ziatni, A. Taitai, Comparative study of artificial neural network and response surface methodology for modelling and op-timization the adsorption capacity of fluoride onto apatitic tricalcium phosphate, Universal Journal of Applied Mathematics 2 (2014) 84–91.

[55] F. Geyikçi, E. Kılıç, S. Çoruh, S. Elevli, Modelling of lead adsorption from industrial sludge leachate on red mud by using RSM and ANN, Chem. Eng. J. 183 (2012) 53–59.

[56] M. Hadi, G. McKay, M.R. Samarghandi, A. Maleki, M. Solaimany Aminabad,

Prediction of optimum adsorption isotherm: comparison of chi-square and log-likelihood statistics, Desalin. Water Treat. 49 (2012) 81–94.

[57] A. Mesdaghinia, A. Azari, R.N. Nodehi, K. Yaghmaeian, A.K. Bharti, S. Agarwal, V.K. Gupta, K. Sharafi, Removal of phthalate esters (PAEs) by zeolite/Fe3O4: investigation on the magnetic adsorption separation, catalytic degradation and toxicity bioassay, J. Mol. Liq. 233 (2017) 378–390.

[58] C.-Y. Chen, Y.-C. Chung, Removal of phthalate esters from aqueous solutions by chitosan bead, J. Environ. Sci. Health A 41 (2006) 235–248.

[59] E.T. Özer, B. Osman, A. Kara, E. Demirbel, N. Beşirli, Ş. Güçer, Diethyl phthalate removal from aqueous phase using poly (EGDMA-MATrp) beads: kinetic, isothermal and thermodynamic studies, Environ. Technol. 36 (2015) 1698–1706.

[60] Q. Shi, A. Li, Q. Zhou, C. Shuang, Y. Li, Removal of diethyl phthalate from aqueous solution using magnetic iron–carbon composite prepared from waste anion exchange resin, J. Taiwan Inst. Chem. Eng. 45 (2014) 2488–2493.

[61] Z. Wang, Efficient adsorption of dibutyl phthalate from aqueous solution by activated carbon developed from phoenix leaves, Int. J. Environ. Sci. Technol. 12 (2015) 1923–1932.